Jiang and Dickson
Acta Neuropathologica Communications (2025) 13:53
https://doi.org/10.1186/s40478-025-01969-2

Acta Neuropathologica Communications

METHODOLOGY

Open Access

Correlative light and electron microscopy imaging of proteinaceous deposits in cell cultures and brain tissues

Peizhou Jiang[1*] and Dennis W. Dickson[1]

Abstract

Identifying protein deposits and associated components is crucial for understanding the pathogenesis of neurodegenerative disorders with intracellular or extracellular deposits. Correlative light and electron microscopy (CLEM) has emerged as a powerful tool to accurately study tissue and cellular pathology by examination of the same target at both microstructural and ultrastructural levels. However, the technical challenges with CLEM have limited its application to neuropathology. Here, we developed a simplified efficient CLEM method and applied it to a cell model that produces a high proportion of α-synuclein (αS) inclusions with immunopositivity to phosphorylated αS and the synaptic vesicle marker SV2A and synaptophysin. This approach incorporates modifications in sample processing and innovative fiducial marking techniques, which enhance antigen preservation and improve target registration, respectively. These advancements achieve an optimal balance in sensitivity, accuracy, efficiency, and cost-effectiveness compared to current CLEM methods employing different strategies. Using this method, we identified and analyzed αS inclusions in cell cultures, as well as various pathological protein deposits in postmortem brain tissues from individuals with a range of neurodegenerative disorders. Our findings replicate recently reported new features of αS pathology and also reveal unrecognized a variety forms of small αS inclusions in human brain, which provide valuable insights into mechanisms underlying Lewy-related pathology. Application of this enhanced CLEM method is a powerful tool in research on neurodegenerative disorders, including αS-opathies.

Keywords Neurodegenerative disease, Correlative light and electron microscopy (CLEM), Proteinaceous inclusion bodies, Lewy bodies, Senile plaques, Neurofibrillary tangles

Introduction

The presence of protein deposits is a common feature of many neurodegenerative diseases [1–5]. Although these deposits differ in their distribution (e.g., intra- and extracellular spaces, specific cell types, or brain regions) and major components depending on the disease type, their size, quantity, and distribution are often closely correlated with disease severity [6–9]. Despite this, the underlying mechanisms of protein deposit formation and progression remain poorly understood.

Identifying protein deposits and their associated components is a critical step toward understanding the mechanisms of protein deposition. Examining pathological brain tissues with light microscopy (LM) and electron microscopy (EM) have been the most common approach, but these methods require preparing separate samples for LM and EM, leading to the potential mismatch of target regions. This discrepancy raises questions about whether ultrastructural features of protein deposits observed under EM actually correlated with components seen with LM. In this regard, the application

*Correspondence:
Peizhou Jiang
Jiang.Peizhou@mayo.edu
[1] Department of Neuroscience, Mayo Clinic, 4500 San Pablo Road, Jacksonville, FL 32224, USA

of a recently developed technique, correlative light and electron microscopy (CLEM), provides a solution to this problem by ensuring that the observations at both microstructural and ultrastructural levels are from the same target [10–14]. CLEM can reveal previously unidentified forms of protein deposits. For example, the long-standing view that the fibrillar form of aggregated α-synuclein (αS) is the primary constituent of Lewy bodies—a hallmark of Parkinson's disease (PD) and dementia with Lewy bodies (DLB)—was recently challenged with CLEM technology. In this study lipid membrane fragments, distorted organelles, and non-fibrillar forms of αS were reported to be major structural components of Lewy bodies [15]. This underscores the value of CLEM in showing details of protein deposits and associated structures. Despite its advantages, a practical application of CLEM for research laboratories remains a challenge due to technical and logistical difficulties.

Currently, there are three major approaches to CLEM:

1. *Single-section imaging for LM and EM*: In this method, both LM and EM images are obtained from the same section. For some applications, fluorescence cryo-microscopy and electron cryo-microscopy are used sequentially to capture LM and EM images [16–18]. Inother cases, samples undergo high pressure freezing or plunge freezing, freeze substitution, embedding, and sectioning, followed by imaging with integrated fluorescence LM and scanning EM systems, such as SECOM [19–21]. This strategy typically requires cryofixation to preserve robust fluorescent signals (e.g., from endogenous expression or immunostaining) and well-maintained ultrastructure. The sample preparation process is complex, involving painstaking procedures such as cryo-sectioning and freeze substitution. Additionally, the use of cryo-specific equipment, such as cryo-ultramicrotomes, makes this approach costly and time-consuming. A further limitation is the lower resolution of scanning EM in systems like SECOM compared to conventional EM.
2. *Z-stack LM imaging followed by EM processing and imaging*: In this approach, fluorescence-labeled samples are imaged under LM using Z-stack methods to capture multiple focal planes. The sample is then processed into a series of sections for EM imaging [22, 23]. It is worth noting that the inclusion of alphanumeric etched grids represents a time-saving improvement for cell culture studies [24]. Moreover, a recently published protocol fully leveraged this approach, enabling the successful collection of ultrastructural details in human brain tissues [25, 26]. While this method provides high-quality LM images, aligning EM sections precisely with the focal plane of the LM image is challenging. Furthermore, the field of view in EM sections can be difficult to correlated with those from LM images, making registration between modalities a significant hurdle [27–29].
3. *Serial sectioning for imaging of LM and EM separately*: In this method, continuous sections are cut from epoxy resin-embedded samples dividing one part for EM imaging and the other part for immunolabeling (after antigen retrieval) and LM imaging. Correlation between LM and EM images is achieved through matching specific features [15]. Although this method is cost-effective and convenient, its antigen retrieval efficiency is often suboptimal, potentially compromising the results.

Across all strategies, fiducial markers are crucial for registering targets in both LM and EM; however, selecting suitable fiducial markers on sections presents a challenge, further complicating the CLEM workflow [30, 31].

These technical and logistical barriers have hindered widespread application of CLEM, particularly in the study of neurodegenerative diseases. To address these challenges, we developed a simplified and time-efficient CLEM method based on an existing protocol [15] using αS pathology as a model to study protein deposits in cell and tissue samples. By replacing conventional ethanol dehydration with DMSO and substituting hydrophobic epoxy resin with the hydrophilic acrylic resin LR White, this approach enhances fluorescence signal quality in LM images and allows identification of additional forms of proteinaceous deposits (e.g., αS pathology) under EM. These advancements make CLEM more accessible and effective, offering potential to accelerate molecular and structural research on neurodegenerative diseases.

Materials & methods

Cell culture and maintenance

Three cell models based upon the H4 neuroglioma cell line were created. The cells were transfected with wild type αS or homo-oligomeric Tag3 (HoTag3)-tagged αS (H4/αS and H4/αS-HoTag3) as well as a tagged control of Venus-tagged protein (H4/Venus-HoTag3) were used in this study. Cells were maintained in OPTI-MEM medium (Invitrogen) supplemented with 10% fetal bovine serum (Invitrogen) and 5 μg/ml blasticidin. The cultures were incubated at 37 °C. Cells were seeded in medium at a density of 2×10^4 cells per well on coverslips in 24-well plates and harvested prior to reaching 90% confluency for immunocytochemistry. For EM studies of αS inclusions, cells were cultured in 6-well plates and harvested at 100% confluency.

Antibodies

For immunocytochemical staining of cell cultures, primary antibodies were against phosphorylated αS at serine 129 (Cat #: 015-25191, mouse monoclonal, Wako USA, 1:1000), αS (NACP98, rabbit polyclonal, Mayo Clinic, 1:1000) [32], αS (Cat #: NBP2-25,146, Chicken polyclonal, Novus biologicals, 1: 1000, only for Fig. 4B), SV2A (Cat #: PA5-52,476, rabbit polyclonal, Thermo Fisher, 1: 800, for Fig. 4B), and Synaptophysin (Cat #: 17,785-1-AP, rabbit polyclonal, Proteintech, 1:800, for Fig. 4B). For immunofluorescence staining of ultrathin sections, primary antibodies were against αS (NACP98, 1:300), Tau (Catalog # Ab75714, Abcam, chicken polyclonal, 1:300), human Aβ (1-42) (Catalog # AS08329, Alexotech, chicken polyclonal, 1:300) and human Aβ full length (Catalog # 71-5800, Thermo Fisher, rabbit polyclonal, 1:300). Secondary antibodies were goat anti-rabbit IgG(H + L) conjugated with Alexa Fluor™ 488 (Catalog # A-11008, Thermo Fisher, 1:500), goat anti-rabbit IgG(H + L) conjugated with Alexa Fluor™ 594 (Catalog # A-11012, Thermo Fisher, 1:500), goat anti-chicken IgY(H + L) conjugated with Alexa Fluor™ 488 (Catalog # A-11039, Thermo Fisher, 1:500), goat anti-chicken IgY(H + L) conjugated with Alexa Fluor™ 594 (Catalog # A-11042, Thermo Fisher, 1:500), goat anti-mouse IgG(H + L) conjugated with Alexa Fluor™ 594 (Catalog # A-11005, Thermo Fisher, 1:1000) and goat anti-rabbit IgG(H + L) conjugated with Alexa Fluor™ 647 (Catalog # A-21244, Thermo Fisher, 1:1000).

Human brain samples

Post-mortem brain tissues from six patients with confirmed neurodegenerative diseases were obtained from the Brain Bank for Neurodegenerative Disorders at Mayo Clinic Florida. Detailed information regarding postmortem interval, clinical diagnosis, pathological diagnosis, and individual patient-related CLEM results is provided in Supplementary Table 1.

Sample preparation for ultrathin sections for CLEM

Samples were fixed overnight in 4% paraformaldehyde and 0.05% glutaraldehyde in 0.1 M sodium cacodylate buffer (Catalog # 15952-15S, 16539-08 and 11655, Electron Microscopy Sciences). After washing with 1 × PBS, they were post-fixed in 1% osmium tetroxide (OsO_4, Catalog # 19172, Electron Microscopy Sciences) for 60–90 min, washed three times with pure water, and stained with 1% uranyl acetate (UA, Catalog # 22400-1, Electron Microscopy Sciences) for 30 min. Sequential dehydration was performed with 30%, 50% and 75% dimethyl sulfoxide (DMSO, Catalog # 276855, Sigma) once, followed by 90% DMSO twice, each for 10–15 min. Samples were infiltrated with DMSO/LR White at ratios of 1:2 and 1:4 for 1 h each, then placed in pure LR White (Catalog # 14381, Electron Microscopy Sciences) overnight. The next day, samples were embedded in fresh LR White within embedding tubes and polymerized in a vacuum oven at 50 °C for 2 days. To aid in image matching, the sample block surface was trimmed into an irregular trapezoid shape. Ultrathin sections of varying thickness were prepared using a Leica UC7 ultramicrotome (Leica Microsystems).

Image acquisition for LM and EM

Fluorescence light microscopy (LM)

For optimization of embedding media and dehydration reagent, the thickness of LM sections was 150 nm to ensure that samples had sufficient epitopes for effective immunostaining as confirmed in a similar study [15]. After establishing an effective method at this thickness, section thickness was reduced to 120 nm. Ultrathin sections were transferred to gelatin-coated slides and air dried. Epon-embedded sections were treated with sodium ethoxide for 30 min to remove resin (which was not required for LR White). For immunostaining, sections were treated with 10% sodium meta-periodate (Catalog # 20504, Thermo Fisher) for 1 h to remove OsO_4, then probed with primary antibodies overnight at 4 °C, followed with secondary antibodies for 1 h at room temperature. Autofluorescence was quenched with Sudan Black B. After mounting in VECTASHIELD® Antifade Mounting Medium with DAPI (Catalog # H-1200-10, Vector Laboratories), sections were imaged using a Zeiss LSM 880 confocal laser scanning microscope with a 40 × lens (ZEISS Microscopy).

Electron microscopy (EM)

Ultrathin sections (70 nm) were placed on Formvar-coated copper grids (FFGA1500-Cu-50, Electron microscopy sciences), counterstained with UA and lead citrate, and examined with a JEM-1400Flash electron microscope (JEOL Ltd.). By aligning the irregular trapezoid shape of the whole section, the orientation of EM sections could be matched to LM fluorescence images. With the help of fiducial markers, each single target of interest between EM and LM section was readily correlated for imaging.

Immunogold EM

Ultrathin sections (90 nm) were placed onto a Formvar-coated nickel grid (FFGA1500-Ni-50, Electron microscopy sciences), treated with 5% sodium meta-periodate for 30 min, immunostained with primary antibody against αS (NACP98, Mayo Clinic, rabbit polyclonal, 1:50) overnight at 4 °C, and incubated with 12 nm

immunogold-conjugated secondary antibodies (Cat # 111-205-144, Jackson Immuno Research Inc.) for 1 h at room temperature. Sections were then counterstained with UA and lead citrate followed by imaging with EM as described above.

Correlative light and electron microscopy (CLEM)

After imaging was complete, a commercial software named "PhotoPad Image Editor" (NCH software) was used to identify ultrastructural details of each single target by matching EM/LM, IEM/LM, or EM/IEM images. The protein aggregates and the associated components could be localized in the EM image with careful adjustment of the size and orientation between the overlaid images. Final images showing the precise location of region of interest were then generated and exported.

Statistical analysis

Data from at least three independent experiments were analyzed using one-way ANOVA with Dunnett's post hoc test for comparisons of groups larger than two or with Student's *t*-test for two-group comparisons. Statistical significance was determined accordingly.

Results

Establishment of a cell model with high proportion of phosphorylated αS inclusions for CLEM

Identification of Lewy pathology under EM is often a time-consuming process due to the small size of EM samples derived from diseased brain tissues, which frequently lack sufficient inclusions in the limited field of view. Cell cultures with a high proportion of αS inclusions provide a more practical platform for testing new CLEM methods; however, no such commercial cell models currently exist. To address this, we developed the H4/αS-HoTag3 cell model.

The HoTag3 tag is a ~ 30-amino-acid sequence that forms homo-hexamers and is commonly used to induce protein phase separation or multivalent protein–protein interactions [33, 34]. The H4/αS-HoTag3 cell line was developed to stably express the recombinant αS gene fused with the HoTag3 tag at its C-terminus—referred to as "αS-HoTag3" (Fig. 1A, B). To serve as controls, two additional cell models were created: H4/αS and H4/Venus-HoTag3. The H4/αS control expresses αS without any tag, while the H4/Venus-HoTag3 control expresses Venus protein fused with the HoTag3 tag. Both αS-HoTag3 and Venus-HoTag3 were expected to self-oligomerize into hexamers. Although previous studies have shown that HoTag3 induced phase separation of other proteins, such as enhanced green fluorescent protein (EGFP), it does not lead to discernible inclusions in cells [33, 34]. We hypothesized that the intrinsic self-assembly propensity of αS would be enhanced by HoTag3, leading to accelerated aggregation and potentially resulting in visible αS aggregates. As anticipated, immunofluorescence staining for αS revealed that more than 95% of cells in the H4/αS-HoTag3 model formed large αS inclusions. In contrast, no visible αS or Venus inclusions were observed in H4/αS or H4/Venus-HoTag3 cells (Fig. 1C). Furthermore, the inclusions in H4/αS-HoTag3 cells were immunopositive for phosphoserine 129-αS, a hallmark of pathological αS species found in Lewy pathology (Fig. 1C). The high proportion of pathologically relevant inclusions made the H4/αS-HoTag3 cell line an excellent model for exploring CLEM.

Improving antigenic preservation with LR white embedding resin

Effective CLEM requires high-quality images from both EM and fluorescence LM. Achieving this quality is challenging without advanced methods like high-pressure freezing and freeze substitution. Critical membrane preservation is routinely achieved in EM with OsO_4 staining; however this method can significantly decrease epitope integrity [35], reducing the signal with immunofluorescence. One solution is to use sodium meta periodate to remove OsO_4 [36, 37], but antigens are not completely restored by this approach.

Embedding media also play a crucial role in preserving antigens and ultrastructural integrity. Hydrophobic epoxy resins, like Epon and Durcupan, provide excellent structural preservation, but they reduce antigenicity [38, 39]. In contrast, hydrophilic acrylic resins, such as LR White, offer superior antigen protection while maintaining ultrastructural details [40–42]. To test whether LR White is a better embedding medium for CLEM, we compared H4/αS-HoTag3 cells embedded in Epon versus LR White.

Both samples underwent fixation with glutaraldehyde and paraformaldehyde with OsO_4 post-fixation, and ethanol dehydration. EM images showed no significant differences in ultrastructural quality between the two media (see a' vs. b' in Fig. 2A); however, immunofluorescence staining following antigen retrieval was significantly stronger and more αS-positive inclusions were detected in LR White-embedded samples (see a vs. b in Fig. 2A, and B). Thus, LR White embedding was found to significantly improve antigen preservation for fluorescence LM, while maintaining EM image quality, making it a better choice for CLEM.

Replacing ethanol with DMSO for dehydration

Ethanol, a standard reagent for sample dehydration, can partially degrade protein epitopes due to its hydrophobic nature [43, 44]. When combined with additional

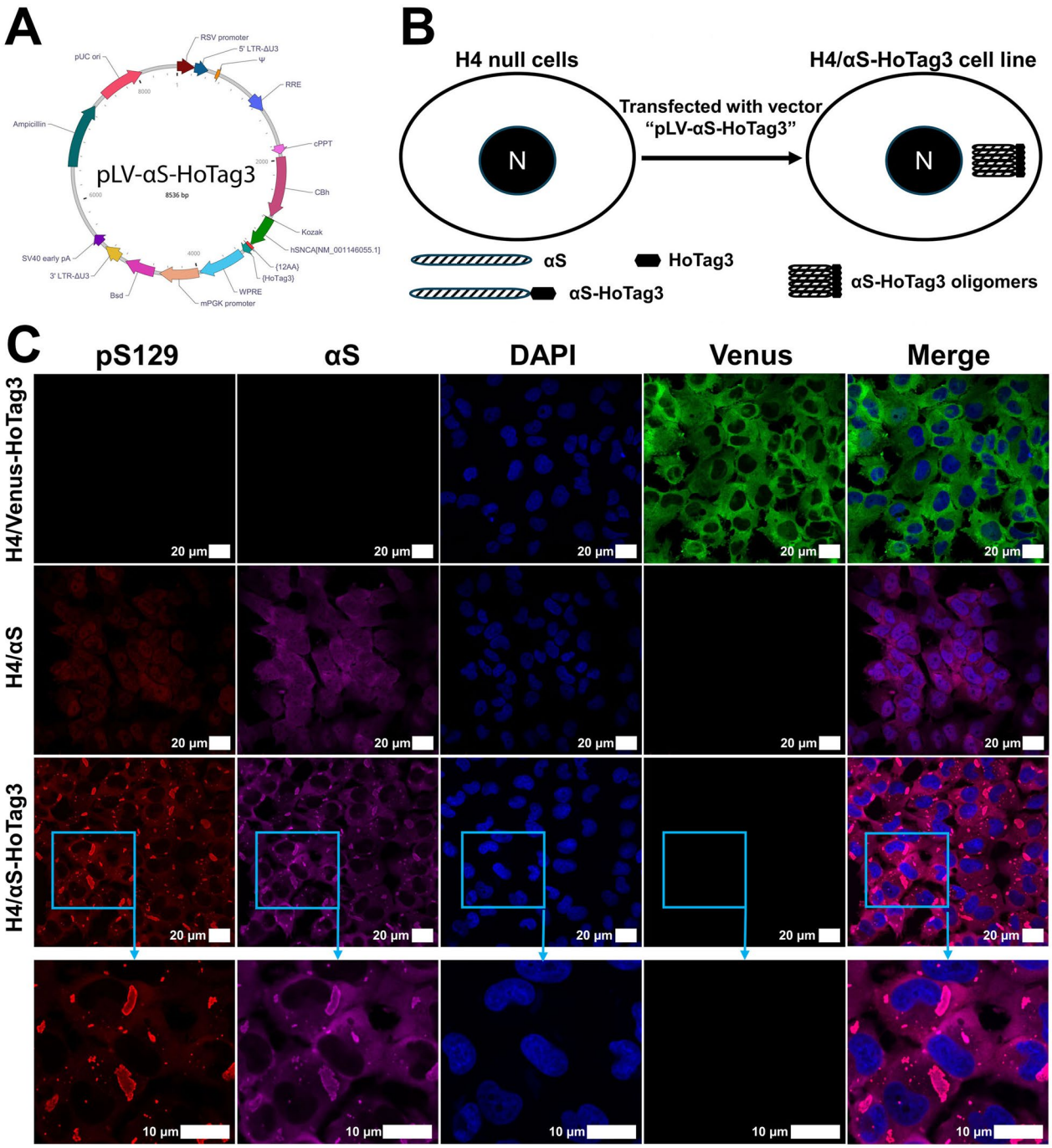

Fig. 1 H4/αS-HoTag3 cell line as a model for CLEM. **A** Map of the plasmid "pLV-αS-HoTag3." The control plasmids, "pLV-αS" and "pLV-Venus-HoTag3," share the same structure, except the gene sequence is replaced with either αS or Venus-HoTag3, respectively. **B** Schematic representation of the establishment of the H4/αS-HoTag3 cell model. H4/αS and H4/Venus-HoTag3 cells were developed using the corresponding control plasmids. **C** Immunofluorescence staining confirms a high proportion of phosphorylated αS (Ser129) inclusions in H4/αS-HoTag3 cells, while these inclusions were absent in the two control cell lines. Scale bars are included in each individual image

antigen-damaging processes such as OsO_4 staining and embedding, significant loss of protein epitopes may occur. This was evident in LR White 100% Ethanol samples (b and b' in Fig. 2), where only ~ 30% of cells retained αS inclusions after antigen retrieval, compared to > 95% retention in cells subjected to fixation

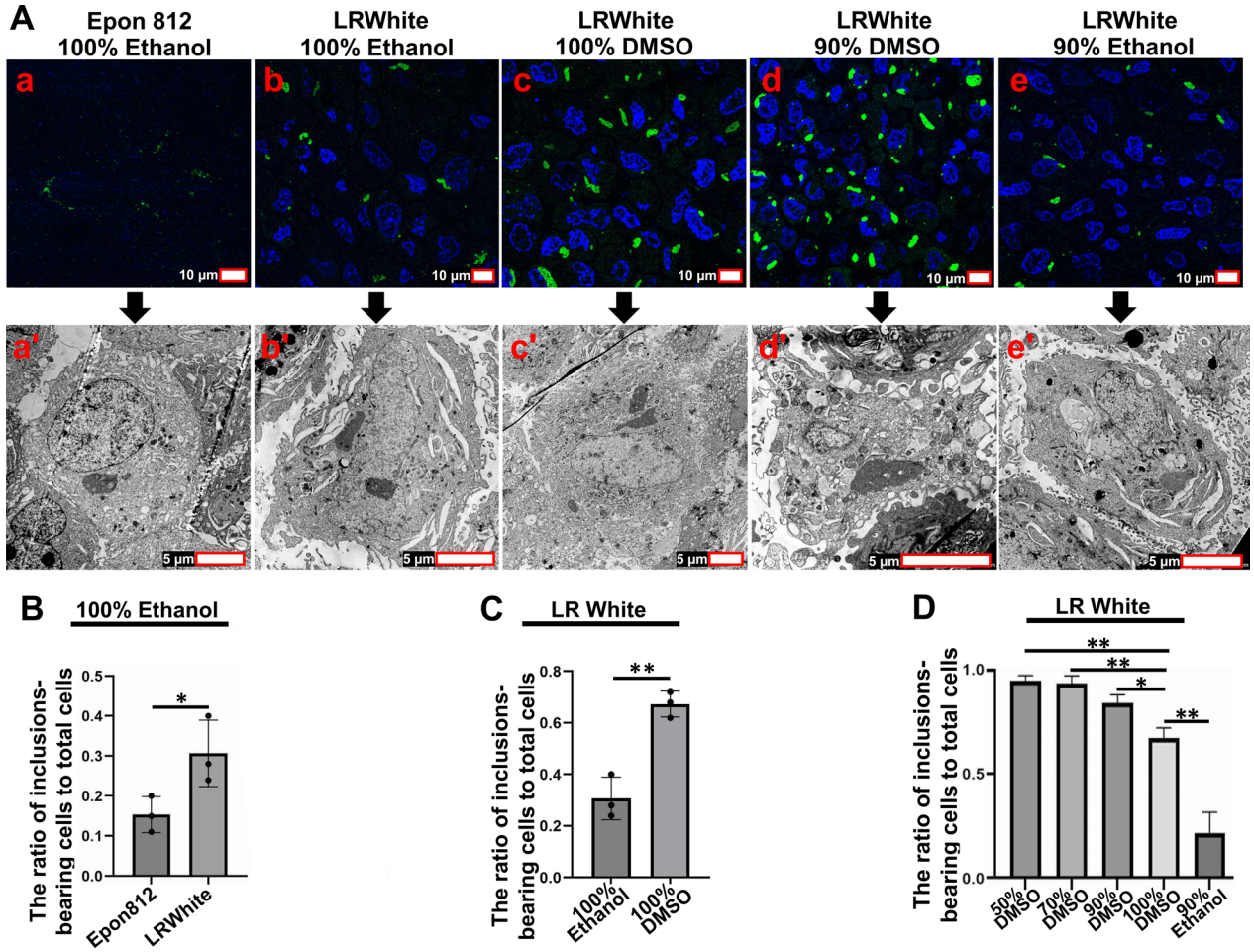

Fig. 2 Samples dehydrated with up to 90% DMSO and embedded in LR White provided significantly better antigen preservation compared to conventional electron microscopy (EM) sample processing. **A** Immunofluorescence staining demonstrated enhanced signal intensity and a greater number of αS inclusions in LR White-embedded samples **b** compared to Epon **a**, in 100% DMSO-dehydrated samples **c** compared to 100% ethanol **b**, in samples dehydrated with up to 90% DMSO **d** compared to both 100% DMSO **c** and 90% ethanol **e**. EM images revealed comparable ultrastructures across these different processing methods, despite their differences in antigen preservation. Scale bars are included in each image. **B** Statistical analysis confirmed that LR White preserves antigens better than Epon. Notably, for Epon-embedded samples, the total number of cells was counted in the immediate ultrathin section under EM, as DAPI staining did not label nuclei. **C** Statistical analysis confirmed that dehydration with dimethyl sulfoxide (DMSO) further enhances antigen preservation compared to ethanol for samples embedded in LR White. **D** Statistical analysis demonstrated that hydrous DMSO (50–90%) preserves antigens better than anhydrous DMSO (100%), with 90% DMSO showing significantly higher antigen preservation than either 100% DMSO or 90% ethanol

and immunocytochemical staining alone, without OsO_4 staining, ethanol dehydration, and embedding (Fig. 1C).

To address this, we evaluated dimethyl sulfoxide (DMSO) as a dehydration agent. DMSO was hypothesized to exhibit potent dehydration capabilities while preserving antigens more effectively than ethanol, owing to its superior tissue penetration properties [45, 46] and cryoprotectant characteristics [45, 47].

H4/αS-HoTag3 cells were subjected to identical fixation and staining protocols, followed by dehydration with ethanol or DMSO. The samples were then embedded in LR White. Immunofluorescence analysis revealed that DMSO-dehydrated samples retained significantly more αS-positive inclusions compared to ethanol-dehydrated samples (see b vs. c in Fig. 2A, C). Notably, there were no detectable differences in ultrastructural quality between the two groups (see b' vs. c' in Fig. 2A). These results confirm that DMSO, with its superior antigenic preservation, is a good alternative to ethanol for dehydration in CLEM applications.

Using 90% DMSO as the final dehydration step

Previous research has shown that limiting dehydration to 70% ethanol enhances antigen retention compared to

higher concentrations of ethanol [48]. To test whether hydrous DMSO could similarly improve antigen preservation compared to its anhydrous form, we processed H4/αS-HoTag3 cells through fixation, OsO_4 post-fixing and UA staining, followed by dehydration up to 50%, 70%, 90% or 100% DMSO. The cells were then embedded in LR White. Ultrathin sections from each group were subjected to antigen retrieval and immunofluorescence staining to evaluate αS expression with fluorescence microscopy.

The results demonstrated varying levels of antigen preservation across the groups. While no statistically significant differences were observed between samples dehydrated with up to 50%, 70% or 90% DMSO, the 100% DMSO group had significantly fewer αS-positive inclusions (Fig. 2D). This indicates that hydrous DMSO offers better antigen preservation than its anhydrous counterpart.

To assess the impact of dehydration on EM image quality, we examined the ultrastructural details of all groups. Samples dehydrated with up to 90% and 100% DMSO yielded comparable EM image quality (see c' vs. d' in Fig. 2A), while those dehydrated with up to 50% or 70% DMSO exhibited poorer contrast and structural sharpness (data not shown). Additionally, a parallel sample dehydrated with up to 90% ethanol confirmed that 90% DMSO provided superior antigen preservation while maintaining comparable EM image quality (see d vs. e, and d' vs. e' in Fig. 2A, and D).

Based on these results, we concluded that dehydration with 90% DMSO offered the best balance of antigen preservation and structural detail for CLEM applications. Consequently, we used 90% DMSO as the final dehydration step before embedding samples in LR White.

CLEM analysis of αS inclusions in cell cultures

Using the improved CLEM sample preparation method as detailed above, we analyzed αS inclusions in H4/αS-HoTag3 cells. Given the superior antigen preservation, we utilized 120 nm sections for immunostaining instead of 150 nm used in previous studies [15], which facilitated improvement in alignment in adjacent sections. To verify alignment, we obtained three continuous sections of 120 nm (left), 70 nm (middle), and 120 nm (right) thickness (Fig. 3). The flanking sections underwent immunostaining for αS, while the middle section was stained with UA and lead citrate for EM imaging.

Results from 20 randomly selected inclusions confirmed precise matching across all three Sections (1A, 2A, 3A in Fig. 3). The use of DAPI-stained nuclei as fiducial markers greatly facilitated target localization on EM Sections (1B and 2B in Fig. 3). The strong immunofluorescence signals further enabled accurate identification of αS inclusions based on their shapes and positions relative to nuclei.

A detailed ultrastructural analysis of at least 100 randomly selected inclusions revealed that αS inclusions in H4/αS-HoTag3 cells predominantly consisted of tightly clustered, small spherical or granular structures, often associated with sparse, large vesicles (Fig. 4A). These vesicles resembled synaptic vesicles based on their size. To confirm their nature, we performed dual immunocytochemical staining using antibodies against αS alongside SV2A or Synaptophysin, both synaptic vesicle markers. Strong colocalization of αS inclusions with these markers was observed, as indicated by white and yellow arrows in Fig. 4B. This finding underscores the involvement of synaptic vesicle-like membranous structures in αS inclusions, which were distinct from autophagosomes due to the absence of discernible mono- or multilayer membranes.

Improved CLEM method is able to detect αS aggregates in human brain

We next sought to demonstrate Lewy-related pathology in brain tissues using CLEM with the improved method. Tissue samples from the substantia nigra or amygdala of postmortem brains from PD or DLB patients were processed using this protocol. Initial experiments utilized two consecutive sections for CLEM analysis. The results confirmed that αS inclusions similar to those in cell cultures could be observed in human brain tissue with Lewy-related pathology. The improved method could be effectively used to identify and characterize pathology by correlating images from consecutive sections.

As shown in Fig. 5, inclusions with strong αS immunofluorescence signals exhibited features characteristic of brainstem-type Lewy bodies, consistent with previous reports [49]. Since the section passed through the dense core, which comprises dense amorphous material, as clearly demonstrated by Lewis et al. [25], only the outer 10-nm-wide radiating fibrils were visible (see the fibrillar structures denoted by white arrowheads in the field marked with a four-pointed red star). These fibrils were surrounded by membranous structures such as lysosomes or neuromelanin. Interestingly, additional αS-immunopositive signals of varying sizes and intensities were detected in the cytoplasm surrounding the dense core. However, not all correlated EM fields contained fibrillar αS aggregates. For example, in the field marked with a five-pointed red star, αS-positive fluorescence signals colocalized with abnormal mitochondrial structures, denoted by black arrowheads in Fig. 5.

To confirm the specificity of these sparsely distributed immunofluorescence signals for αS, we employed an additional "sandwich" method, as illustrated in Fig. 6. One

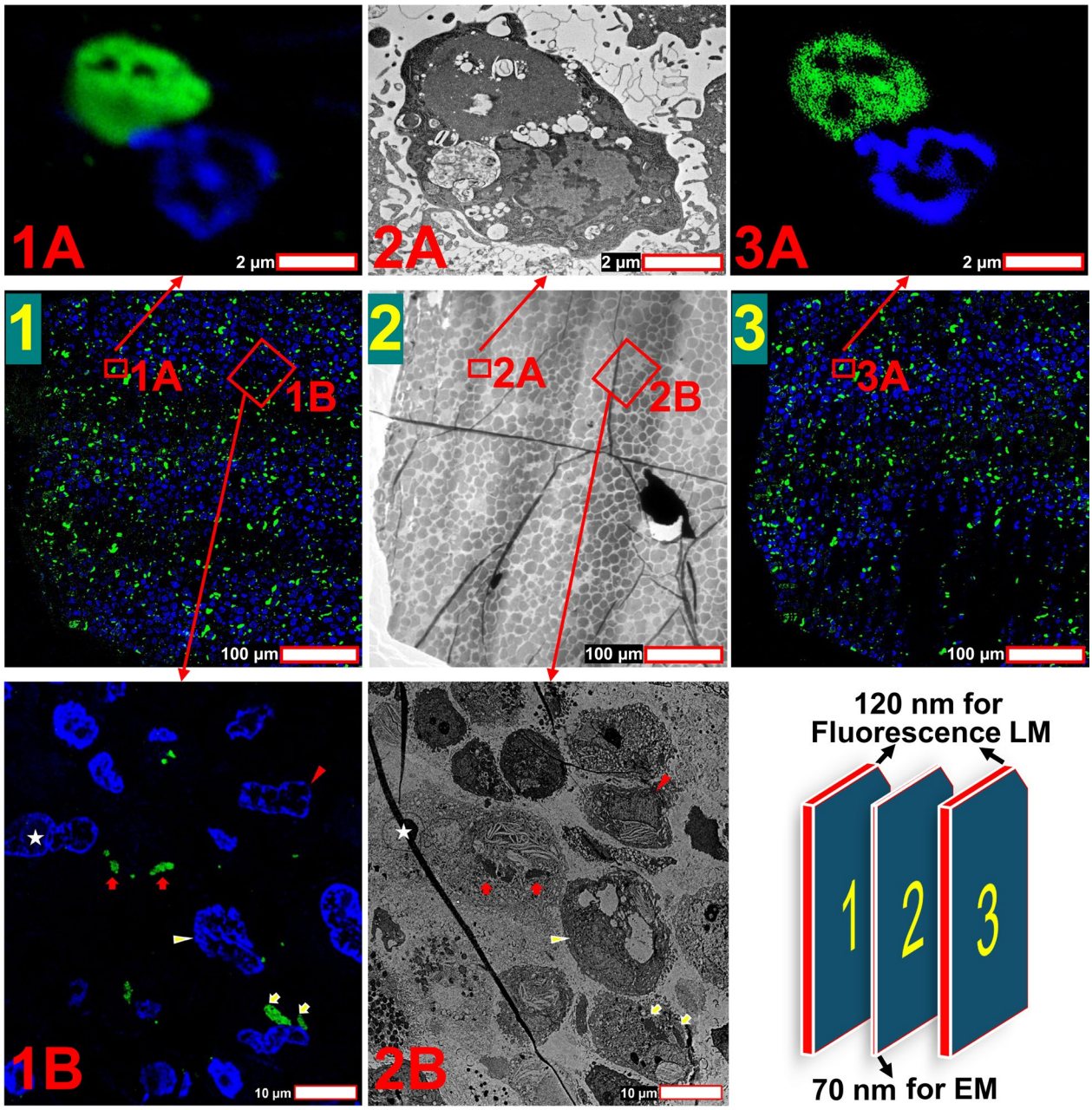

Fig. 3 Precise matching across continuous sections *(Top)* Images of immunofluorescence (1A/3A) and EM (2A) from three continuous sections demonstrate accurate alignment of αS inclusions in a single cell, aided by DAPI-stained nuclei. *(Middle)* Whole-section views confirm alignment between three continuous sections (1/2/3). Framed fields are respectively enlarged into corresponding images on top and at bottom. *(Bottom)* The left two enlarged images (1B/2B) highlight αS inclusions and nuclei as fiducial markers. Arrows and arrowhead of the same color respectively denoted the αS inclusions and nuclei in the same cells on different section. *Note*: the white asterisk pointed at a folded area occasionally occurring on the 70 nm section, which should be avoided for CLEM analysis. A sketch map showing the thickness of three continuous sections is on the right. Scale bars are included in each individual image

side of a 120-nm-thick section was used for immunofluorescence staining for αS, while the opposite side (90 nm thick) was placed on a nickel grid for immunogold labeling of αS. The images from LM and immuno-EM were successfully overlaid by matching the same EM image in the middle 70-nm section. This approach enabled precise correlation of all αS-immunofluorescence signals to their exact locations in the immuno-EM images.

We first examined the location corresponding to a large Lewy body with the highest immunofluorescence signal

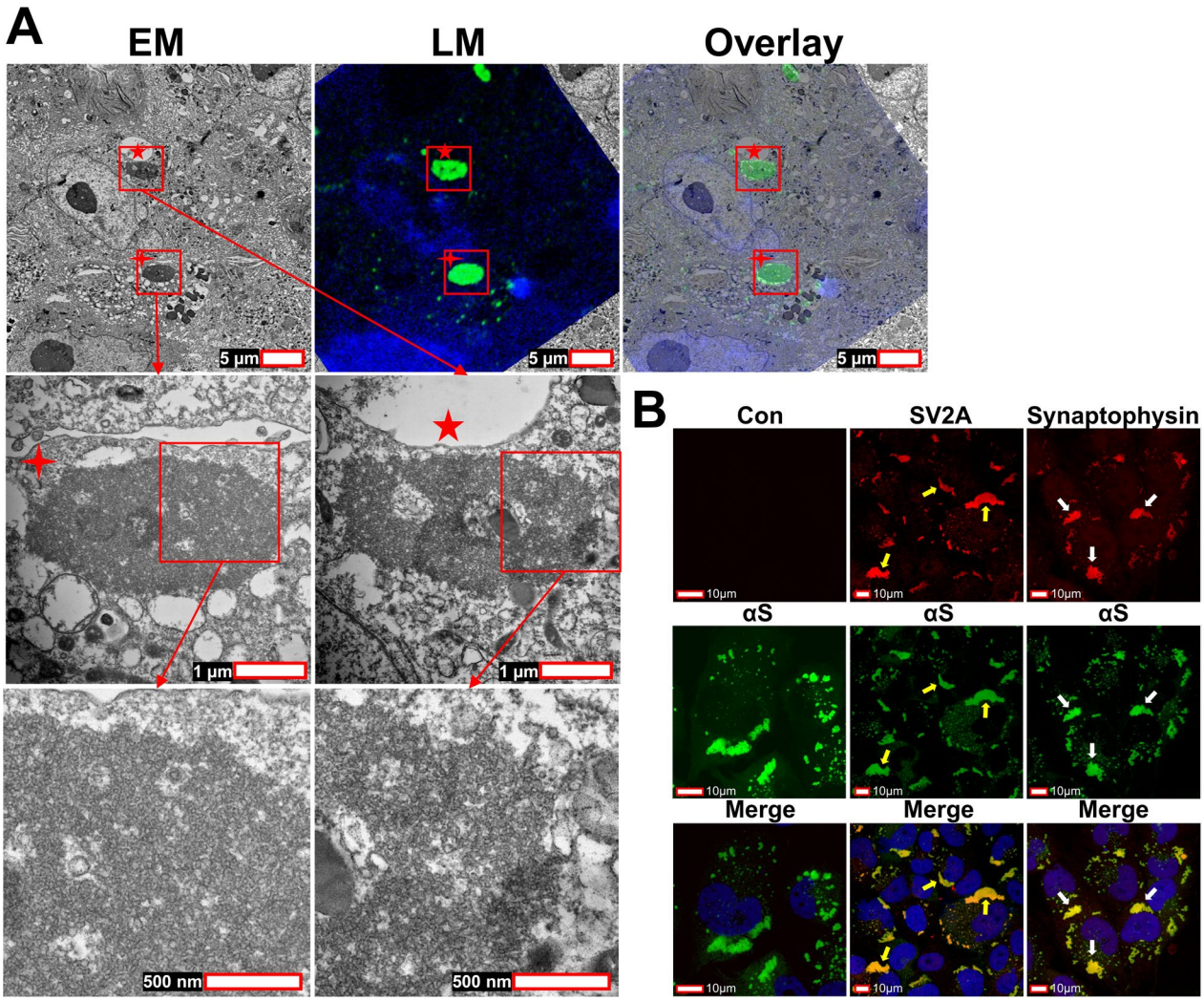

Fig. 4 Ultrastructural characteristics of αS inclusions in H4/αS-HoTag3 cells. **A** High-resolution EM image upon matching with LM image reveal tightly clustered spherical structures and vesicles in αS inclusions. The selected inclusions are respectively marked with 4 or 5-pointed red stars, and then enlarged to the corresponding images in the next row, where a part of the structures is framed and further enlarged to images in another row. **B** Immunocytochemical staining of H4/αS-HoTag3 cells with antibodies against αS, along with SV2A or Synaptophysin, revealed the colocalization of αS inclusions with both synaptic vesicle markers. This colocalization was absent in control cells subjected to the same staining, except for the omission of primary antibodies against SV2A or Synaptophysin. Yellow and white arrows indicate representative inclusions showing the colocalization of αS with SV2A and αS with Synaptophysin, respectively. Scale bars are included in each individual image

intensity. In this area, we identified predominantly fibrillar αS aggregates densely labeled with immunogold particles (denoted by red arrowheads in subframe 3 of the field marked with a four-pointed red star in Fig. 6A). Next, we randomly inspected fields corresponding to sparsely distributed immunofluorescence signals. These regions also displayed immunolabeled gold particles, with densities varying according to the form of the αS aggregate. For example, in the fields marked with a five-pointed red star and subframes 1 and 2, we observed membrane-associated structures that were labeled with immunogold particles (denoted by black arrowheads in subframes 1 and 2 of Fig. 6A). In comparison, the density of gold particles on non-fibrillar αS aggregates was less than that in fibrillar aggregates (compare subframes 1 and 2 with subframe 3), consistent with the differences observed in immunofluorescence intensity between the two forms. These findings confirmed the specificity of sparsely distributed immunofluorescence signals for αS aggregates. Moreover, our observations suggest that immunofluorescence signal intensity may serve as a reference for predicting fibrillar or non-fibrillar forms of αS aggregates.

These results demonstrate that the improved CLEM method enhances the ability to identify αS aggregates in

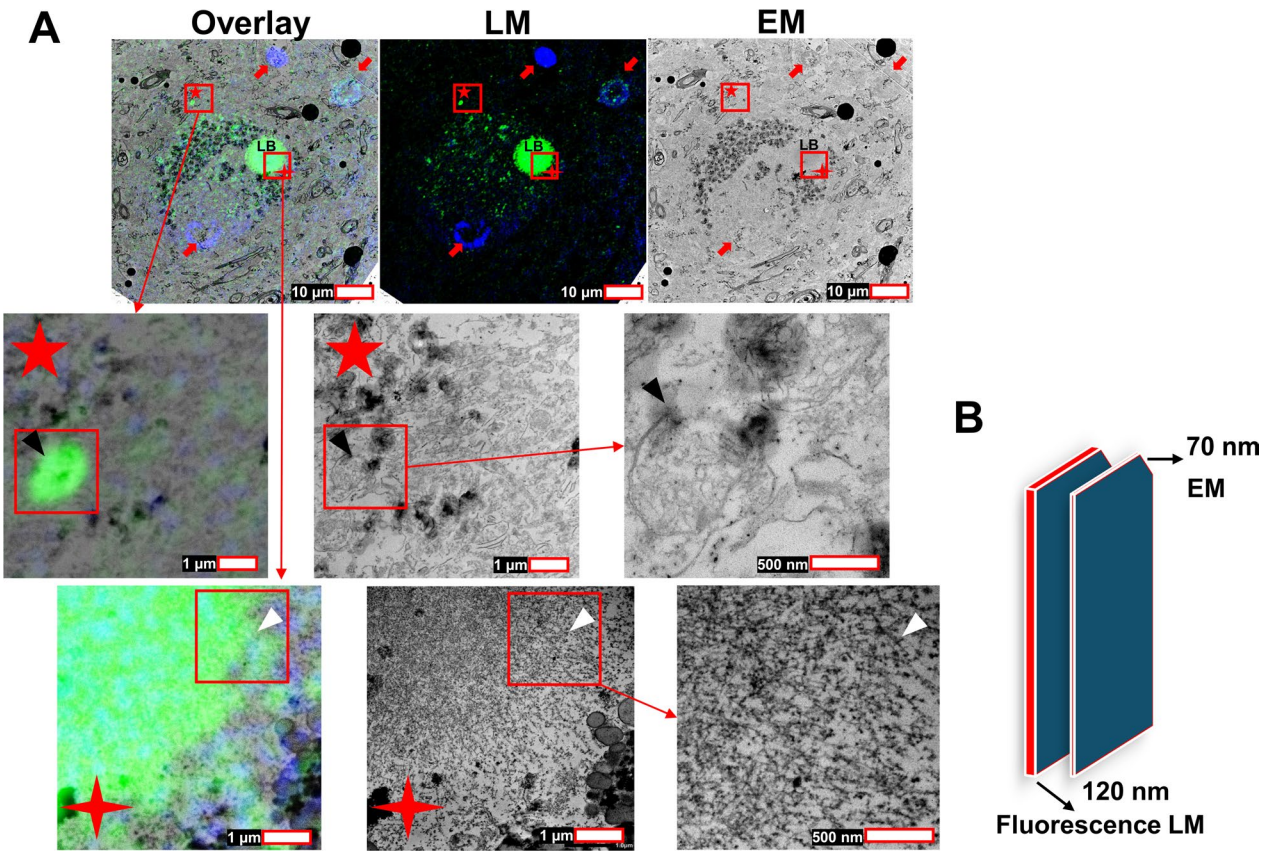

Fig. 5 Identification of a classical Lewy body in human brain tissues. **A** A brainstem-type Lewy body (marked as LB) was readily identified using CLEM, aided by the fiducial marker—DAPI-stained nuclei (denoted by red arrows). Several small αS aggregates of varying sizes were also observed in the cytoplasm surrounding the large Lewy body. A portion of the Lewy body (four-pointed red star) and αS aggregate-associated structures (five-pointed red star) are framed in the top images and magnified in the next row. White and black arrowheads denote radiating αS fibrils and non-fibrillar αS-associated structures, respectively. Scale bars are included in each image. **B** A schematic illustrates the differences in thickness between two immediate sections

brain tissues, ranging from classical Lewy bodies to small sparse fibrils and non-fibrillar structures. This capability underscores the value of CLEM for studying heterogeneity of αS aggregates in human neurodegenerative disorders.

Identification of diverse αS aggregates

Further analysis of PD brain sections revealed that our improved CLEM method can detect numerous small αS inclusions ranging from 100 to 500 nm in size (Figure S1–S4).

A preliminary examination of these inclusions identified four distinct types of non-fibrillar αS aggregates in neurons: (1) condensed membranous structures (denoted by red arrows in Figure S1), occasionally incorporating organelles like mitochondria (red arrowheads in Figure S1); (2) loosely associated vesicles and organelles (red arrows and arrowheads in Figure S2); (3) lysosome-like structure-associated aggregates (red arrows and arrowheads in Figure S3); and (4) unmyelinated axon bundles (red arrows and arrowheads in Figure S4). These findings expand our understanding of α-synuclein pathology and highlight the heterogeneity of αS aggregates.

Application to Alzheimer's disease (AD)

The improved CLEM method was also applied to Alzheimer's disease (AD) tissues. We first performed dual immunofluorescence staining on the same section using antibodies against Aβ and tau from different host species, allowing for the simultaneous visualization of deposits from both proteins, which are characteristic of AD pathology [50]. As shown in Fig. 7, Aβ-immunopositive regions in the LM images (red fluorescence signals) corresponded to clusters or scattered amyloid fibrils, appearing as loose or compact fibrillar bundles under EM (see images magnified from green-framed fields). Interestingly, tau-immunopositive pathological structures were also detected in the same area of the LM image

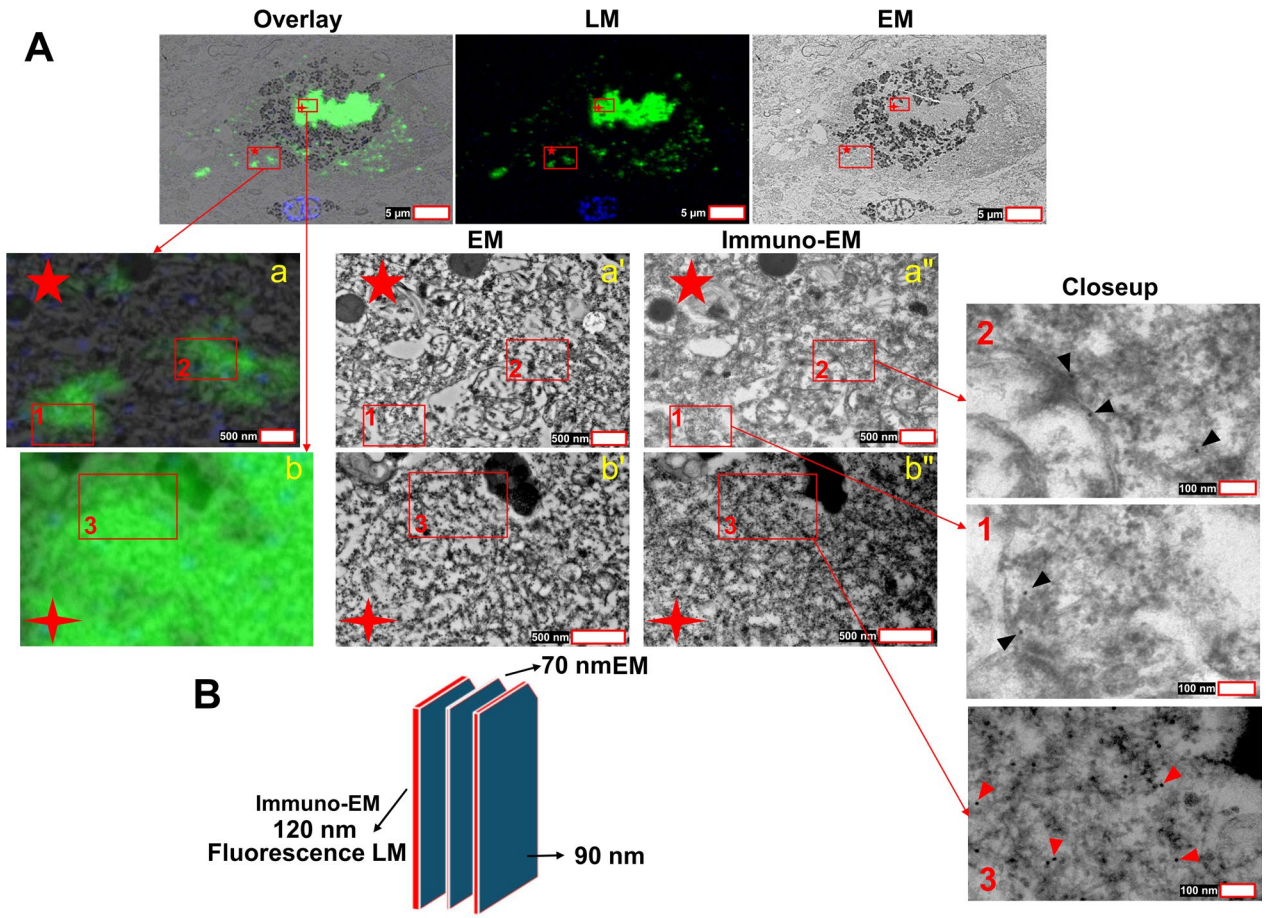

Fig. 6 Precise localization of α-synuclein aggregates using the sandwich CLEM method. **A** The ultrastructure of αS aggregates of varying sizes and forms surrounding a Lewy body was identified by correlating immunofluorescence signals with corresponding EM images. Non-fibrillar αS-associated structures (five-pointed red star) and fibrillar αS within a portion of the Lewy body (four-pointed red star) are marked in the top row. These regions are further displayed in magnified images of LM/EM overlay (**a**, **b**), EM (**a'**, **b'**), and immuno-EM (**a''**, **b''**), where three subframes (1, 2, and 3) highlight the precise localization of αS in various forms. Subframes 1 and 2, selected from fields with sparsely distributed αS-immunopositive fluorescence signals (**a**, **a'**, **a''**), are further magnified in the column labeled "Close-up," revealing membrane-associated non-fibrillar αS aggregates, clearly labeled by immunogold particles (black arrowheads). In contrast, subframe 3, selected from a field with intense αS-immunopositive fluorescence signals (**b**, **b'**, **b''**), demonstrates predominantly fibrillar αS aggregates labeled with immunogold particles (red arrowheads). Scale bars are provided in each image. **B** A schematic illustrates thickness differences among the three consecutive sections used in the sandwich CLEM method

(green fluorescence signals). EM analysis revealed these as bundles of 20-nm-wide paired helical filaments, with a distinct twisted ribbon-like structure visible at higher magnifications (see images magnified from blue-framed fields). Both pathologies are consistent with previously reported features of senile plaques and neurofibrillary tangles, the hallmark lesions of AD [51–54].

In cases where antibody host species limitations prevented dual staining, we employed a modified sandwich method using three consecutive sections. As shown in Fig. 8, Aβ-immunopositive (red fluorescence signals) and tau-immunopositive (green fluorescence signals) pathologies were demonstrated in the two outer sections stained with antibodies from the same host species (chicken). By correlating these with the central EM section, we integrated the separate fluorescence images into a single overlay, allowing for simultaneous localization of both pathologies. EM analysis further revealed their ultrastructural details, with amyloid fibrils visible in the blue-framed field and neurofibrillary tangles in the yellow-framed field. This approach enabled the simultaneous identification of multiple targets, providing a comprehensive view of AD pathology.

These results demonstrated that the improved CLEM method can be effectively extended beyond α-synucleinopathies to study other neurodegenerative

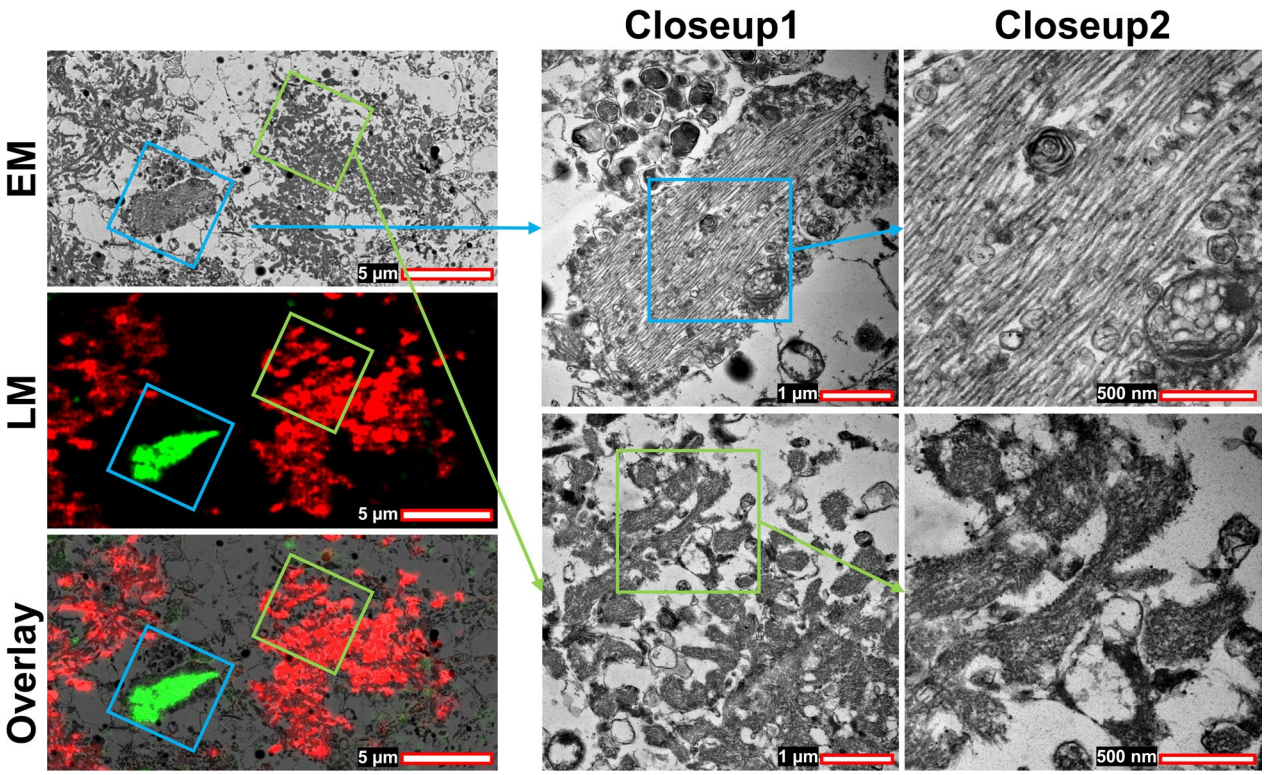

Fig. 7 CLEM identification of senile plaques and neurofibrillary tangles on the same EM section using dual immunofluorescence staining. Two immediate ultrathin sections, 120 nm and 70 nm thick, were obtained from embedded AD brain tissue. The 120 nm section underwent immunofluorescence staining with primary antibodies against Tau (chicken-derived) and Aβ (rabbit-derived), followed by secondary antibodies conjugated with Alexa Fluor™ 488 goat anti-chicken (green signal) and Alexa Fluor™ 594 goat anti-rabbit (red signal). The 70 nm section was subjected to UA and lead staining to generate EM images. CLEM was used to align the fluorescence LM signals with the ultrastructural EM details, allowing visualization of senile plaques and neurofibrillary tangles in the EM image. Framed regions in the left images are magnified in closeup1, and further detailed enlargements are presented in closeup2. Scale bars are included in all images

proteinopathies. Furthermore, it enables the simultaneous investigation of multiple pathological hallmarks within the same brain tissue section, enhancing our ability to correlate immunofluorescence and ultrastructural findings.

Discussion

Although CLEM has demonstrated significant benefits in neurodegenerative disease research, its application remains limited to a small number of laboratories due to the obstacles outlined in the introduction. In the present study, we developed an improved method for CLEM that could be used for both cell cultures and postmortem human tissue samples. The key improvements of our method over conventional CLEM approaches, based on the three strategies described in the introduction, are summarized in Table 1.

First, our method enhances antigenicity preservation during sample processing, building on an existing cost-effective and convenient approach [15]. Second, we successfully adapted the method for multiplex immunostaining on the same or adjacent sections, enabling the use of CLEM to detect multiple pathologies within a single sample. Third, we significantly reduced the time and complexity of the CLEM workflow by replacing hydrophobic epoxy resin (e.g., Epon) with hydrophilic acrylic resin (e.g., LR White) for embedding which rendered sections suitable for counterstaining with DAPI, providing clear visualization of nuclei and facilitating their use as fiducial markers. This greatly simplifies the registration of targets of interest on EM sections. We believe these improvements make CLEM more user-friendly and accessible, and suggest that these methods may promote broader application of CLEM in neurodegenerative disease research.

To gain more ultrastructural details and identify additional pathological structures from EM sections, we describe a novel "sandwich method" for CLEM, combining three continuous ultrathin sections. This method can be modified to suit various research purposes. For instance, it can be used with a combination of 120 nm, 70 nm, and 90 nm sections (Fig. 6), where the two outer

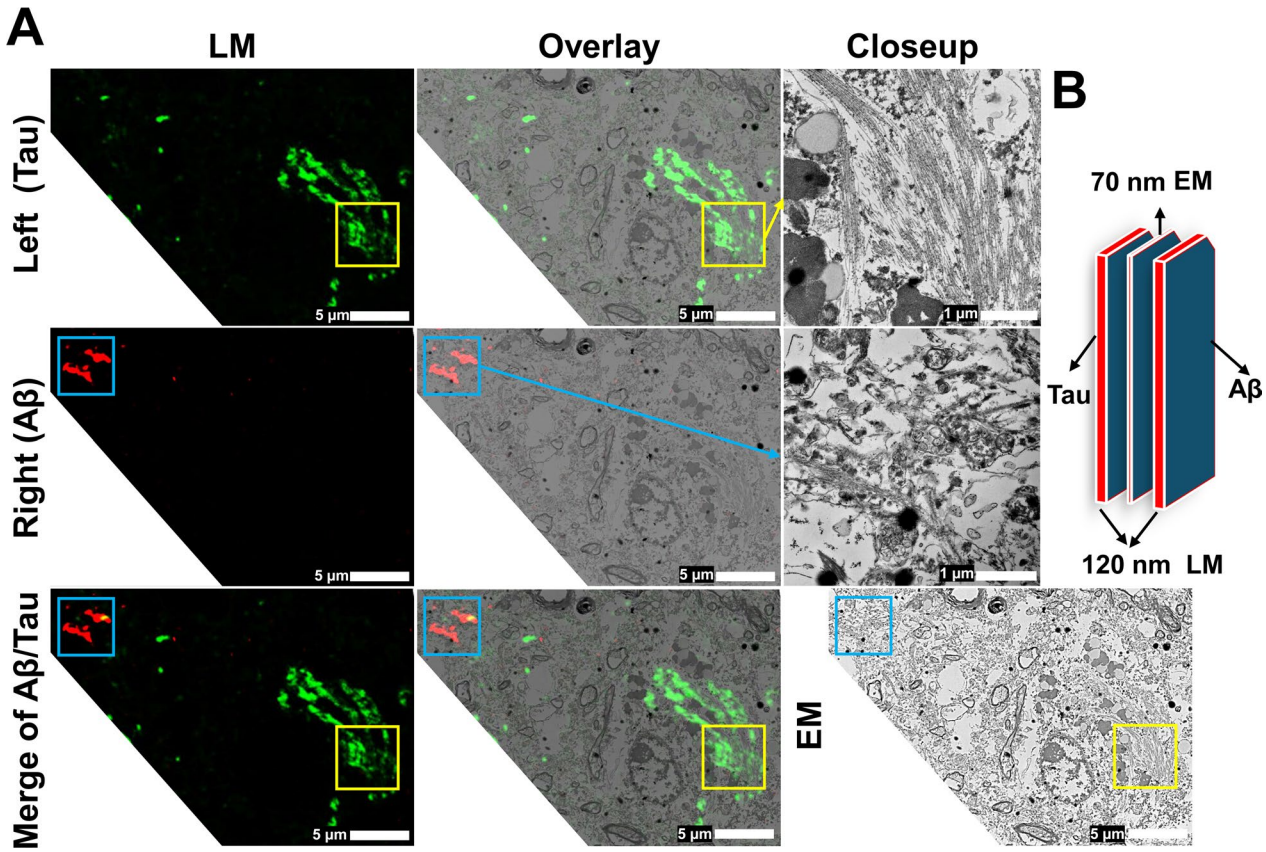

Fig. 8 CLEM sandwich method for identifying senile plaques and neurofibrillary tangles using single immunofluorescence staining on flanking ultrathin sections. **A** Three consecutive sections, 120 nm, 70 nm, and 120 nm thick, were obtained. The two 120 nm flanking sections were stained with chicken-derived primary antibodies against Tau and Aβ, respectively. Secondary antibodies conjugated with Alexa Fluor™ 488 goat anti-chicken (green signal) and Alexa Fluor™ 594 goat anti-chicken (red signal) were used to generate fluorescence LM images for Tau and Aβ. The middle 70 nm section was subjected to UA-lead staining for EM imaging. Each fluorescence LM image (for Tau or Aβ) was matched with the EM image to generate individual CLEM overlays (left flanking section for Tau and right for Aβ). These individual CLEM images were further merged to create a combined overlay, displaying both senile plaques and neurofibrillary tangles in the same image. Framed regions in the overlay images are enlarged for more detailed visualization in the closeup images. Scale bars are included in all images. **B** A schematic diagram illustrates the thickness differences among the three consecutive sections

sections are subjected to immunofluorescence staining (120 nm) and immunogold labeling (90 nm), respectively. This approach permitted (1) mapping the overall distribution of targets of interest (e.g., αS) on the 120 nm section using immunofluorescence staining, (2) revealing the ultrastructural details of the targets on the central 70 nm section using UA/lead staining, and (3) precisely localizing the targets on the 90 nm section using immunogold labeling (Fig. 6A).

In other configurations using 120 nm, 70 nm, and 120 nm sections (Fig. 8), the two outer sections were stained with different antibodies targeting distinct molecules. By aligning the images from these sections with the middle EM section, we could merge data to demonstrate all targets on a single CLEM image. Although in this study the sandwich method was only applied to detect two different types of pathology using antibodies from the same host species, it can be extended to identify more targets simultaneously. For example, when immunofluorescence staining is applied to the two outer sections, and each section is probed with antibodies from three different host species (assuming antibody availability is not an issue), up to six targets could theoretically be detected. In contrast, due to the overlapping size distributions of commercial immunogold particles with adjacent sizes [55], it is recommended to distinguish at most two different targets using immunogold particles of significantly different sizes to avoid potential misinterpretation. Nevertheless, this sandwich method significantly broadens applications of CLEM, particularly in studies of neurodegenerative diseases involving multiple proteinopathies.

We first applied the improved method to identify αS inclusions in both cell cultures and brain tissues. The results clearly demonstrated the intracellular distribution

Table 1 Comparison of the strengths and limitations between our method and other conventional methods

Comparison for CLEM application	Strategy I	Strategy II	Strategy III	
	Single-section imaging	*Z-stack LM imaging/ EM processing & imaging*	*Serial sections for separately imaging of LM and EM*	*Our improved method*
Quality of LM image 1	+ + +	+ + + + +	+	+ +
Quality of EM image 2	+ + + +	+ + + + +	+ + + + +	+ + + + +
Section alignment and overlay accuracy 3	+ + + + +	+	+ + + +	+ + + +
Technical friendliness 4	+	+ + +	+ + + + +	+ + + + +
Simplicity in sample process 5	+	+ + +	+ + + + +	+ + + + +
Fiducial markers usage 6	+ + + + +	+ + + + +	NA	+ + + + +
Multiplex staining for LM image 7	+ + + + +	+ + + + +	NA	+ + + +
Integration with immuno-EM 8	NA	NA	NA	+ + + + +

1—Strategy II captures the original immunofluorescence signal without additional processing, while Strategy I requires cryo-processing, which theoretically preserves antigenicity better than the antigen retrieval process used in Strategy III. However, our method in Strategy III demonstrates superior antigenicity preservation compared to traditional approaches

2—Strategy I does not use OsO_4 staining, resulting in lower contrast in EM images compared to Strategies II and III

3— Strategy I employs a single section for both LM and EM, ensuring the best overlay accuracy. Strategy II relies on Z-stack imaging for LM, which can be challenging to align with the cutting plane of the EM section. In contrast, Strategy III utilizes immediately adjacent sections for LM and EM, significantly minimizing overlay errors. This approach is effective as long as the EM section has no folded areas or the folded regions (e.g., as shown in image 2B of Fig. 3) are excluded from analysis

4—Strategy I and some experiments in Strategy II require high-pressure freezing and freeze substitution

5—Strategy I Involves delicate manipulation for cryo-processing, and Strategy II requires embedding samples in situ

6—Strategy III (prior to our method) did not utilize fiducial markers, which are now incorporated in our improved approach

7—Strategy III (prior to our method) did not perform multiplex staining on ultrathin sections, a feature now enabled by our method

8—Our method introduces the novel integration of immuno-EM into CLEM, significantly enhancing its capabilities

and ultrastructural features of αS inclusions, achieved through precise matching of the target and fiducial markers between EM and fluorescence LM images based on their unique shapes and sizes. In H4/αS-HoTag3 cells, αS inclusions appeared as tightly clustered membranous structures (Fig. 4), resembling αS aggregate-induced formations observed in presynaptic terminals of certain αS transgenic animals [56–58]. Notably, these inclusions were immunopositive for both αS pSer129, a marker for pathological αS, and SV2A plus Synaptophysin, two synaptic vesicle markers (Fig. 1C, 4B). This suggests that the inclusions may result from αS aggregation-induced clustering of synaptic vesicles and similar structures, consistent with previous reports that αS promotes synaptic vesicle clustering [59]. In brain tissues with Lewy pathology, αS inclusions had different ultrastructural features, appearing either as membrane-associated structures (e.g., vesicles of various sizes or lysosome-associated structures) or as fibrillar structures (Figs. 5 and 6, S1–S4). Importantly, we did not observe any inclusions in brain tissues resembling those found in H4/αS-HoTag3 cells, which may be due to the limited number of cases and selected regions examined. On the other hand, since clustered presynaptic vesicles are thought to associate with αS aggregates at early stage in the synucleinopathy pathological cascade [57], it is plausible that the αS inclusions in H4/αS-HoTag3 cells are analogous to precursors of Lewy bodies. Consistent with most cell models overexpressing αS, H4/αS-HoTag3 cells did not form fibrillar structures within the αS inclusions. This may result from the non-senescent nature of immortalized cell lines, which lack the unique microenvironment of the human brain that promotes αS fibril formation. While animal models are generally more suitable than cell models for testing techniques intended for use with human post-mortem material, animals expressing αS in the brain—unlike those expressing Tau or Aβ [60–63]—rarely self-generate αS fibrils unless induction with exogenous preformed fibrils [64]. Therefore, H4/αS-HoTag3 cells, which can self-generate a high proportion of αS inclusions, became our optimal choice for this study. It would be intriguing to investigate whether αS-HoTag3 expressed in animal brains could form fibrillar αS during aging. If confirmed, this would support the hypothesis that Lewy pathology progresses through distinct stages, with membranous structure-associated, non-fibrillar αS aggregates potentially serving as precursors to fibrillar inclusions at later stages.

Using this improved method, we identified numerous αS inclusions significantly smaller (100–500 nm) than classical Lewy pathology (8–30 μm in diameter) [65]. Ultrastructural analysis revealed that most of these inclusions were non-fibrillar αS aggregates, primarily falling into four categories. In addition to the previously characterized crowded membranous organelles described by Shahmoradian et al. [15], we found non-fibrillar αS

tightly associated with (1) loose vesicles and organelles, (2) lysosome-like structures, and (3) unmyelinated axons bundles. The enhanced sensitivity of our CLEM method, attributed to superior antigen preservation, likely enabled the detection of a broader range of αS aggregate forms in ultrathin EM sections. Interestingly, lysosome-associated structures frequently exhibited αS immunopositivity and emerged as a major form of Lewy pathology, supporting the hypothesis that lysosomes play a crucial role in αS aggregation [66, 67]. It is important to note that these four types of αS inclusions were identified through a preliminary examination of small αS aggregates during CLEM analysis of PD brain tissue. A more comprehensive study is necessary to fully characterize the nature and diversity of these inclusions. Additionally, whether these small αS inclusions eventually accumulate to form larger Lewy pathology remains unclear, warranting further investigation in future studies.

Beyond α-synucleinopathies, this improved method has proven valuable for studying other neurodegenerative pathologies. For example, CLEM analysis of AD brain tissue successfully identified both senile plaques and neurofibrillary tangles in matched EM and fluorescence LM images (Figs. 7, 8). The consistency of these ultrastructural details with prior reports in the literature further validates the reliability of our CLEM method. These observations, coupled with the identification of novel forms of αS aggregate, suggest that improved CLEM methods hold potential for uncovering previously unrecognized pathological features and pathological combinations in neurodegenerative diseases.

A limitation of this study is that fluorescence signals for CLEM can only be generated through fluorescence staining on ultrathin sections. It is unlikely that fluorescence signals could be directly observed in samples containing endogenously expressed or exogenous fluorescent substances, as any fluorescence signal is likely to be extinguished during postfixation staining with OsO_4 and subsequent dehydration with DMSO. To address this, using high pressure freezing/freeze-substitution or Cryo-EM to preserve inner fluorescence signals in embedded samples, or capturing fluorescence LM images before embedding, remain the two main strategies for CLEM when targeting endogenous fluorescence-labeled structures. On the other hand, just as DMSO serves as a dehydration reagent that preserves antigens better than the conventional ethanol, it may be possible to find alternative reagents that more effectively preserves fluorescence signals as well as lipid integrity. This will be the focus of our future work.

Another limitation involves the selection of antibodies for immunostaining. While monoclonal antibodies, due to their specificity for single epitopes, are generally preferable for targeting proteins of interest, ultrathin sections present unique challenges. The limited availability of epitopes in these sections means that polyclonal antibodies, which can target multiple epitopes, remain the preferred reagent. Despite significant improvement in antigen preservation achieved by our method, it did not fully resolve this issue. As such, we recommend using polyclonal antibodies for immunostaining on ultrathin sections. This observation also suggests that αS-immunofluorescence signals observed in LM images are unlikely to originate from monomeric αS. This can be further confirmed by comparing immunocytochemical results on cell cultures (Figs. 1, 4B) with immunofluorescence results on ultrathin sections (Figs. 2, 3, 4A). In Figs. 1 and 4B, both αS inclusions and the cytoplasmic regions were successfully immunostained with the αS antibody. In contrast, in ultrathin sections of the same cultures, immunofluorescence signals were limited to αS inclusions and sparsely distributed small puncta, while the cytoplasmic regions—presumably containing at least homo-hexameric αS—showed no fluorescence signals. Therefore, our method is primarily suitable for identifying protein deposits or other structures with a high concentration of epitopes.

Conclusion

In summary, we have developed an improved method for sample processing and fiducial marker labeling in CLEM, which significantly enhances antigen preservation and target registration compared to conventional methods using ethanol dehydration and epoxy resin embedding. These advancements achieve an optimal balance in sensitivity, accuracy, efficiency, and cost-effectiveness compared to current CLEM methods employing different strategies. Using this improved method, we successfully identified and analyzed αS inclusions in cell cultures, as well as various pathological protein deposits in post-mortem brain tissues from individuals with different neurodegenerative diseases. Some of these findings have provided valuable insights into the mechanisms underlying the pathogenesis of Lewy-related pathologies. We believe that this improved method can significantly broaden access to CLEM technology for laboratories with conventional transmission electron microscopy, thereby contributing to advancing research in neurodegenerative diseases and related fields.

Supplementary Information

The online version contains supplementary material available at https://doi.org/10.1186/s40478-025-01969-2.

Additional file 1: Figure S1. CLEM identification of condensed membranous structure-associated αS inclusions. In the top panels (A, B), αS inclusions are highlighted by frames and denoted by red arrows. These regions

are magnified in the corresponding bottom-row images. The right images in the bottom row further enlarge the framed areas on the left, revealing that fields with intense green fluorescence signals are primarily filled with condensed membranous structures. Occasionally, αS-negative organelles, such as mitochondria, were sequestered within these inclusions (B, denoted by a red arrowhead). Scale bars are included in each image.

Additional file 2: Figure S2. CLEM identification of αS inclusions as loose vesicle- and organelle-associated structures. In the top row, αS aggregates in different locations are framed and denoted by red arrows and arrowheads, respectively. These regions are magnified in the bottom-row images. Areas with strong green fluorescence signals predominantly contained loose vesicles and organelles. Scale bars are included in each image.

Additional file 3: Figure S3. CLEM identification of lysosome-like structures-associated αS inclusions. In the top row, αS inclusions in different location are respectively framed and denoted by arrows and arrowhead, which are further magnified in the bottom row images. Fields with intense green fluorescence signals primarily comprise lysosome-associated materials, such as lysosomes or lipofuscin-like structures. Scale bars are included in each image.

Additional file 4: Figure S4. CLEM identification of clustered axon-associated αS inclusions. A distinctive type of αS aggregate forming a ring structure is shown in the top-row images. Two regions within this structure are framed and denoted by red arrows and arrowheads, which are further magnified in the next row. These fields, marked by intense green fluorescence signals, contain unmyelinated axons bundles. Scale bars are included in each image.

Additional file 5

Acknowledgements
The authors thank Monica Castanedes-Casey, Nathan S. Perez, Nikhil B. Ghayal and Alexia R. Maier for support for histology.

Author contributions
P.J. designed and conducted all experiments and authored the manuscript. D.D. provided valuable guidance on pathological identification and contributed to revising the manuscript.

Funding
This study was supported in part by the National Institute of Health grants (U54 NS110435; U01 NS100620, U19 AG069701, P01 AG003949), the Mangurian Foundation Lewy Body Dementia Program at Mayo Clinic, and the Mayo Foundation for Medical Education and Research.

Availability of data and materials
Not applicable.

Declarations

Ethics approval and consent to participate
All brain autopsies were conducted with consent from the next-of-kin or individuals with legal authority to grant permission for brain autopsy. Protocols for brain bank operations were approved by the Mayo Clinic Institutional Review Board.

Consent for publication
Not applicable.

Competing interests
The authors declare that they have no competing interests.

Received: 6 January 2025 Accepted: 20 February 2025
Published online: 08 March 2025

References

1. Koo EH, Lansbury PT Jr, Kelly JW (1999) Amyloid diseases: abnormal protein aggregation in neurodegeneration. Proc Natl Acad Sci U S A 96:9989–9990. https://doi.org/10.1073/pnas.96.18.9989
2. Kumar V, Sami N, Kashav T, Islam A, Ahmad F, Hassan MI (2016) Protein aggregation and neurodegenerative diseases: from theory to therapy. Eur J Med Chem 124:1105–1120. https://doi.org/10.1016/j.ejmech.2016.07.054
3. Ross CA, Poirier MA (2004) Protein aggregation and neurodegenerative disease. Nat Med 10:S10-17. https://doi.org/10.1038/nm1066
4. Shastry BS (2003) Neurodegenerative disorders of protein aggregation. Neurochem Int 43:1–7. https://doi.org/10.1016/s0197-0186(02)00196-1
5. Sweeney P, Park H, Baumann M, Dunlop J, Frydman J, Kopito R, McCampbell A, Leblanc G, Venkateswaran A, Nurmi A et al (2017) Protein misfolding in neurodegenerative diseases: implications and strategies. Transl Neurodegener 6:6. https://doi.org/10.1186/s40035-017-0077-5
6. Braak H, Braak E (1995) Staging of Alzheimer's disease-related neurofibrillary changes. Neurobiol Aging 16:271–278. https://doi.org/10.1016/0197-4580(95)00021-6
7. Braak H, Ghebremedhin E, Rub U, Bratzke H, Del Tredici K (2004) Stages in the development of Parkinson's disease-related pathology. Cell Tissue Res 318:121–134. https://doi.org/10.1007/s00441-004-0956-9
8. Brettschneider J, Del Tredici K, Toledo JB, Robinson JL, Irwin DJ, Grossman M, Suh E, Van Deerlin VM, Wood EM, Baek Y et al (2013) Stages of pTDP-43 pathology in amyotrophic lateral sclerosis. Ann Neurol 74:20–38. https://doi.org/10.1002/ana.23937
9. Wanker EE (2000) Protein aggregation and pathogenesis of Huntington's disease: mechanisms and correlations. Biol Chem 381:937–942. https://doi.org/10.1515/BC.2000.114
10. Bykov YS, Cortese M, Briggs JA, Bartenschlager R (2016) Correlative light and electron microscopy methods for the study of virus-cell interactions. FEBS Lett 590:1877–1895. https://doi.org/10.1002/1873-3468.12153
11. de Boer P, Hoogenboom JP, Giepmans BN (2015) Correlated light and electron microscopy: ultrastructure lights up! Nat Methods 12:503–513. https://doi.org/10.1038/nmeth.3400
12. Iwasaki H, Ichinose S, Tajika Y, Murakami T (2022) Recent technological advances in correlative light and electron microscopy for the comprehensive analysis of neural circuits. Front Neuroanat 16:1061078. https://doi.org/10.3389/fnana.2022.1061078
13. Kremer A, Lippens S, Guérin CJ (2016) Correlative light and electron microscopy: methods and applications. In: eLS, John Wiley & Sons, Ltd (Ed): https://doi.org/10.1002/9780470015902.a0025983
14. Loussert Fonta C, Humbel BM (2015) Correlative microscopy. Arch Biochem Biophys 581:98–110. https://doi.org/10.1016/j.abb.2015.05.017
15. Shahmoradian SH, Lewis AJ, Genoud C, Hench J, Moors TE, Navarro PP, Castano-Diez D, Schweighauser G, Graff-Meyer A, Goldie KN et al (2019) Lewy pathology in Parkinson's disease consists of crowded organelles and lipid membranes. Nat Neurosci 22:1099–1109. https://doi.org/10.1038/s41593-019-0423-2
16. Schellenberger P, Kaufmann R, Siebert CA, Hagen C, Wodrich H, Grunewald K (2014) High-precision correlative fluorescence and electron cryo microscopy using two independent alignment markers. Ultramicroscopy 143:41–51. https://doi.org/10.1016/j.ultramic.2013.10.011
17. Strnad M, Elsterova J, Schrenkova J, Vancova M, Rego RO, Grubhoffer L, Nebesarova J (2015) Correlative cryo-fluorescence and cryo-scanning electron microscopy as a straightforward tool to study host-pathogen interactions. Sci Rep 5:18029. https://doi.org/10.1038/srep18029
18. Tuijtel MW, Koster AJ, Jakobs S, Faas FGA, Sharp TH (2022) Author Correction: Correlative cryo super-resolution light and electron microscopy on mammalian cells using fluorescent proteins. Sci Rep 12:10897. https://doi.org/10.1038/s41598-022-15037-5
19. Baatsen P, Gabarre S, Vints K, Wouters R, Vandael D, Goodchild R, Munck S, Gounko NV (2021) Preservation of fluorescence signal and imaging optimization for integrated light and electron microscopy. Front Cell Dev Biol 9:737621. https://doi.org/10.3389/fcell.2021.737621
20. Peddie CJ, Blight K, Wilson E, Melia C, Marrison J, Carzaniga R, Domart MC, O'Toole P, Larijani B, Collinson LM (2014) Correlative and integrated light and electron microscopy of in-resin GFP fluorescence, used to localise diacylglycerol in mammalian cells. Ultramicroscopy 143:3–14. https://doi.org/10.1016/j.ultramic.2014.02.001

21. Peddie CJ, Domart MC, Snetkov X, O'Toole P, Larijani B, Way M, Cox S, Collinson LM (2017) Correlative super-resolution fluorescence and electron microscopy using conventional fluorescent proteins in vacuo. J Struct Biol 199:120–131. https://doi.org/10.1016/j.jsb.2017.05.013
22. Boing C, Di Fabrizio M, Burger D, Bol J, Huisman E, Rozemuller AJM, van de Berg WDJ, Stahlberg H, Lewis AJ (2024) Distinct ultrastructural phenotypes of glial and neuronal alpha-synuclein inclusions in multiple system atrophy. Brain 147:3727–3741. https://doi.org/10.1093/brain/awae137
23. Casares-Arias J, Alonso MA, San Paulo A, Gonzalez MU (2021) Correlative confocal and scanning electron microscopy of cultured cells without using dedicated equipment. STAR Protoc 2:100727. https://doi.org/10.1016/j.xpro.2021.100727
24. Hanson HH, Reilly JE, Lee R, Janssen WG, Phillips GR (2010) Streamlined embedding of cell monolayers on gridded glass-bottom imaging dishes for correlative light and electron microscopy. Microsc Microanal 16:747–754. https://doi.org/10.1017/S1431927610094092
25. Lewis AJ vdHL, di Fabrizio M, Burger D, Huisman E, Bol JGJM, van de Berg WDJ, Stahlberg H (2024) Ultrastructural diversity of alpha-Synuclein pathology in the post-mortem brain of Parkinson patients: implications for Lewy Body formation. bioRxiv 07.25.605088 https://doi.org/10.1101/2024.07.25.605088
26. Shafiei NSD, Burger D, Di Fabrizio M, van den Heuvel L, Daraspe J, Böing C, Shahmoradian SH, van de Berg WDJ, Genoud C, Stahlberg H, Lewis AJ (2024) Correlative light and electron microscopy for human brain and other biological models. bioRxiv: 06.11.598271 https://doi.org/10.1101/2024.06.11.598271
27. Ariotti N, Hall TE, Parton RG (2017) Correlative light and electron microscopic detection of GFP-labeled proteins using modular APEX. Methods Cell Biol 140:105–121. https://doi.org/10.1016/bs.mcb.2017.03.002
28. Reddick LE, Alto NM (2012) Correlative light and electron microscopy (CLEM) as a tool to visualize microinjected molecules and their eukaryotic sub-cellular targets. J Vis Exp 4:e3650. https://doi.org/10.3791/3650
29. Santarella-Mellwig R, Haselmann U, Schieber NL, Walther P, Schwab Y, Antony C, Bartenschlager R, Romero-Brey I (2018) Correlative light electron microscopy (CLEM) for tracking and imaging viral protein associated structures in cryo-immobilized cells. J Vis Exp. https://doi.org/10.3791/58154
30. Fathima A, Quintana-Cataño CA, Heintze C, Schlierf M (2021) Precision of fiducial marker alignment for correlative super-resolution fluorescence and transmission electron microscopy. Discov Mater 1:11. https://doi.org/10.1007/s43939-021-00011-1
31. Mohammadian S, Fokkema J, Agronskaia AV, Liv N, de Heus C, van Donselaar E, Blab GA, Klumperman J, Gerritsen HC (2019) High accuracy, fiducial marker-based image registration of correlative microscopy images. Sci Rep 9:3211. https://doi.org/10.1038/s41598-019-40098-4
32. Dickson DW, Liu W, Hardy J, Farrer M, Mehta N, Uitti R, Mark M, Zimmerman T, Golbe L, Sage J et al (1999) Widespread alterations of alpha-synuclein in multiple system atrophy. Am J Pathol 155:1241–1251. https://doi.org/10.1016/s0002-9440(10)65226-1
33. Mumford TR, Rae D, Brackhahn E, Idris A, Gonzalez-Martinez D, Pal AA, Chung MC, Guan J, Rhoades E, Bugaj LJ (2024) Simple visualization of submicroscopic protein clusters with a phase-separation-based fluorescent reporter. Cell Syst 15(166–179):e167. https://doi.org/10.1016/j.cels.2024.01.005
34. Zhang Q, Huang H, Zhang L, Wu R, Chung CI, Zhang SQ, Torra J, Schepis A, Coughlin SR, Kornberg TB et al (2018) Visualizing dynamics of cell signaling in vivo with a phase separation-based kinase reporter. Mol Cell 69(334–346):e334. https://doi.org/10.1016/j.molcel.2017.12.008
35. Roth J, Bendayan M, Carlemalm E, Villiger W, Garavito M (1981) Enhancement of structural preservation and immunocytochemical staining in low temperature embedded pancreatic tissue. J Histochem Cytochem 29:663–671. https://doi.org/10.1177/29.5.6166664
36. Bendayan M, Zollinger M (1983) Ultrastructural localization of antigenic sites on osmium-fixed tissues applying the protein A-gold technique. J Histochem Cytochem 31:101–109. https://doi.org/10.1177/31.1.6187796
37. Yamashita S (2020) Antigen retrieval for light and electron microscopy. Immunohistochem Ageless Biotechnol. https://doi.org/10.5772/intechopen.80837
38. Luft JH (1961) Improvements in epoxy resin embedding methods. J Biophys Biochem Cytol 9:409–414. https://doi.org/10.1083/jcb.9.2.409
39. Yamashita S, Okada Y (2014) Heat-induced antigen retrieval in conventionally processed Epon-embedded specimens: procedures and mechanisms. J Histochem Cytochem 62:584–597. https://doi.org/10.1369/0022155414537899
40. Frankl A, Mari M, Reggiori F (2015) Electron microscopy for ultrastructural analysis and protein localization in *Saccharomyces cerevisiae*. Microb Cell 2:412–428. https://doi.org/10.15698/mic2015.11.237
41. Krenacs T, Ivanyi B, Bozoky B, Laszik Z, Krenacs L, Razga Z, Ormos J (1991) Postembedding Immunoelectron Microscopy with Immunogold-Silver Staining (Igss) in Epon 812, Durcupan Acm and Lr-White Resin Embedded Tissues. J Histotechnol 14:75–80. https://doi.org/10.1179/his.1991.14.2.75
42. Sakai Y, Hosaka M, Hira Y, Watanabe T (2005) Addition of phosphotungstic acid to ethanol for dehydration improves both the ultrastructure and antigenicity of pituitary tissue embedded in LR White acrylic resin. Arch Histol Cytol 68:337–347. https://doi.org/10.1679/aohc.68.337
43. Morita T, Westh P, Nishikawa K, Koga Y (2012) Effects of ethanol and dimethyl sulfoxide on the molecular organization of H_2O as probed by 1-propanol. J Phys Chem B 116:7328–7333. https://doi.org/10.1021/jp303619q
44. Otali D, Stockard CR, Oelschlager DK, Wan W, Manne U, Watts SA, Grizzle WE (2009) Combined effects of formalin fixation and tissue processing on immunorecognition. Biotech Histochem 84:223–247. https://doi.org/10.3109/10520290903039094
45. Lovelock JE, Bishop MW (1959) Prevention of freezing damage to living cells by dimethyl sulphoxide. Nature 183:1394–1395. https://doi.org/10.1038/1831394a0
46. Rammler DH, Zaffaroni A (1967) Biological implications of DMSO based on a review of its chemical properties. Ann N Y Acad Sci 141:13–23. https://doi.org/10.1111/j.1749-6632.1967.tb34861.x
47. Hochstrat E, Muller M, Frank A, Michel P, Hansen U, Raschke MJ, Kronenberg D, Stange R (2019) Cryopreservation of tendon tissue using dimethyl sulfoxide combines conserved cell vitality with maintained biomechanical features. PLoS ONE 14:e0215595. https://doi.org/10.1371/journal.pone.0215595
48. Otali D, He Q, Stockard CR, Grizzle WE (2013) Preservation of immunorecognition by transferring cells from 10% neutral buffered formalin to 70% ethanol. Biotech Histochem 88:170–180. https://doi.org/10.3109/10520295.2012.754496
49. Spillantini MGCR, Jakes R, Hasegawa M, Goedert M (1998) alpha-Synuclein in filamentous inclusions of Lewy bodies from Parkinson's disease and dementia with lewy bodies. Proc Natl Acad Sci U S A 95:6469–6473. https://doi.org/10.1073/pnas.95.11.6469
50. Bloom G (2014) Amyloid-beta and tau: the trigger and bullet in Alzheimer disease pathogenesis. JAMA Neurol 71:505–508. https://doi.org/10.1001/jamaneurol.2013.5847
51. Bamburg JR, Bloom GS (2009) Cytoskeletal pathologies of Alzheimer disease. Cell Motil Cytoskeleton 66:635–649. https://doi.org/10.1002/cm.20388
52. Giaccone GMM, Moda F, Botta M, Mazzoleni G, Uggetti A, Catania M, Moro ML, Redaelli V, Spagnoli A, Rossi RS, Salmona M, Di Fede G, Tagliavini F (2010) Neuropathology of the recessive A673V APP mutation: Alzheimer disease with distinctive features. Acta Neuropathol 120:803–812. https://doi.org/10.1007/s00401-010-0747-1
53. Ferrer I (2023) The unique neuropathological vulnerability of the human brain to aging. Ageing Res Rev 87:101916. https://doi.org/10.1016/j.arr.2023.101916
54. Tosoni A, Barbiano di Belgiojoso G, Nebuloni M (2011) Electron microscopy in the diagnosis of amyloidosis. Amyloidosis - Mechanisms and prospects for therapy. IntechOpen. https://doi.org/10.5772/19102
55. Yi H, Leunissen J, Shi G, Gutekunst C, Hersch S (2001) A novel procedure for pre-embedding double immunogold-silver labeling at the ultrastructural level. J Histochem Cytochem 49:279–284. https://doi.org/10.1177/002215540104900301
56. Scott DA, Tabarean I, Tang Y, Cartier A, Masliah E, Roy S (2010) A pathologic cascade leading to synaptic dysfunction in alpha-synuclein-induced neurodegeneration. J Neurosci 30:8083–8095. https://doi.org/10.1523/JNEUROSCI.1091-10.2010
57. Spinelli KJ, Taylor JK, Osterberg VR, Churchill MJ, Pollock E, Moore C, Meshul CK, Unni VK (2014) Presynaptic alpha-synuclein aggregation in a

mouse model of Parkinson's disease. J Neurosci 34:2037–2050. https://doi.org/10.1523/JNEUROSCI.2581-13.2014
58. Totterdell S, Hanger D, Meredith GE (2004) The ultrastructural distribution of alpha-synuclein-like protein in normal mouse brain. Brain Res 1004:61–72. https://doi.org/10.1016/j.brainres.2003.10.072
59. Diao J, Burre J, Vivona S, Cipriano DJ, Sharma M, Kyoung M, Sudhof TC, Brunger AT (2013) Native alpha-synuclein induces clustering of synaptic-vesicle mimics via binding to phospholipids and synaptobrevin-2/VAMP2. Elife 2:e00592. https://doi.org/10.7554/eLife.00592
60. Beckman D, Chakrabarty P, Ott S, Dao A, Zhou E, Janssen WG, Donis-Cox K, Muller S, Kordower JH, Morrison JH (2021) A novel tau-based rhesus monkey model of Alzheimer's pathogenesis. Alzheimers Dement 17:933–945. https://doi.org/10.1002/alz.12318
61. Lewis J, McGowan E, Rockwood J, Melrose H, Nacharaju P, Van Slegtenhorst M, Gwinn-Hardy K, Paul Murphy M, Baker M, Yu X et al (2000) Neurofibrillary tangles, amyotrophy and progressive motor disturbance in mice expressing mutant (P301L) tau protein. Nat Genet 25:402–405. https://doi.org/10.1038/78078
62. Metaxas A, Thygesen C, Kempf SJ, Anzalone M, Vaitheeswaran R, Petersen S, Landau AM, Audrain H, Teeling JL, Darvesh S et al (2019) Ageing and amyloidosis underlie the molecular and pathological alterations of tau in a mouse model of familial Alzheimer's disease. Sci Rep 9:15758. https://doi.org/10.1038/s41598-019-52357-5
63. Sanchez-Varo R, Sanchez-Mejias E, Fernandez-Valenzuela JJ, De Castro V, Mejias-Ortega M, Gomez-Arboledas A, Jimenez S, Sanchez-Mico MV, Trujillo-Estrada L, Moreno-Gonzalez I et al (2021) Plaque-associated oligomeric amyloid-beta drives early synaptotoxicity in APP/PS1 mice hippocampus: ultrastructural pathology analysis. Front Neurosci 15:752594. https://doi.org/10.3389/fnins.2021.752594
64. Tarutani A, Hasegawa M (2024) Ultrastructures of alpha-Synuclein filaments in synucleinopathy brains and experimental models. J Mov Disord 17:15–29. https://doi.org/10.14802/jmd.23213
65. Outeiro TF, Koss DJ, Erskine D, Walker L, Kurzawa-Akanbi M, Burn D, Donaghy P, Morris C, Taylor JP, Thomas A et al (2019) Dementia with Lewy bodies: an update and outlook. Mol Neurodegener 14:5. https://doi.org/10.1186/s13024-019-0306-8
66. Volta M (2024) Roles of neuronal lysosomes in the etiology of Parkinson's disease. Neural Regen Res 19:1981–1983. https://doi.org/10.4103/1673-5374.390954
67. Xie YX, Naseri NN, Fels J, Kharel P, Na Y, Lane D, Burre J, Sharma M (2022) Lysosomal exocytosis releases pathogenic alpha-synuclein species from neurons in synucleinopathy models. Nat Commun 13:4918. https://doi.org/10.1038/s41467-022-32625-1

Publisher's Note